The International Journal of Advanced Manufacturing Technology (2024) 134:497–509
https://doi.org/10.1007/s00170-024-14075-9

ORIGINAL ARTICLE

The change of the absorptance at the transition from partial-to full-penetration laser welding

Jonas Wagner[1] · Christian Hagenlocher[1] · Rudolf Weber[1] · Thomas Graf[1]

Received: 28 January 2024 / Accepted: 25 June 2024 / Published online: 22 July 2024

Abstract
Full-penetration laser welding processes are necessarily associated with significant changes of the geometrical properties of the keyhole at the beginning of the process when the keyhole expands all the way through the workpiece and finally pierces the bottom of the sheet. The impact that this transition has on the absorptance was investigated by means of X-ray imaging to determine the geometry of the keyhole and subsequent raytracing to calculate the distribution of the absorbed irradiance. The results show a significant drop of the overall absorptance when the bottom of the capillary opens through the rear side of the workpiece which in practice is noticed by an unstable behavior of the keyhole. Since the drop of the absorptance is less pronounced for smaller diameters of the keyhole, one may recommend the application of laser beams with small diameters at least during the initial phase until the keyhole is fully developed and reliably reaches through the bottom surface of the welded sheet.

Keywords Laser beam welding · Aluminum alloy · Absorptance · Keyhole · Full penetration · Partial penetration · Raytracing · X-ray analysis

1 Introduction

Full-penetration laser welding is characterized by a weld seam whose depth equals the material thickness as shown in Fig. 1b. Two modes of full-penetration welding can be distinguished: *Mode A* with a keyhole length less than the thickness of the sheet, as shown on the left in Fig. 1b. And *Mode B*, with a keyhole length equal to the thickness of the sheet, piercing the bottom of the sheet and resulting in a second opening at its bottom, as shown on the right Fig. 1b [1]. The fact that the weld seam is visible from both sides also facilitates the post-process quality assurance because it can be visually ascertained whether or not the required penetration depth was achieved [2]. Compared to the partial-penetration laser welding shown in Fig. 1a, and to full-penetration welding in *mode A*, full-penetration welding with a keyhole that is opened at its bottom (*mode B*) is associated with a more stable keyhole as the additional opening at the bottom prevents potential collapses of the tip of the keyhole [3–5]. The full-penetration process starts in the same manner as the partial-penetration process. The heat input from the laser beam melts the solid material and local vaporization leads to the formation of a keyhole whose length increases while its pressure displaces the surrounding melt. The final length of the keyhole mainly depends on the power of the laser beam, its diameter, and the welding speed [6, 7]. In order to attain full-penetration welding in *mode B*, as depicted in Fig. 1b, with a given beam diameter and speed, the laser power has to be sufficiently high to form a keyhole with a length that equals the thickness of the welded sheets, resulting in a second opening of the keyhole at the rear side of the sheet.

The formation of the additional opening of the keyhole at the transition to welding in full-penetration *mode B* coincides with an abrupt reduction of the area which the laser beam irradiates, as indicated by the red areas in Fig. 1, and an increase of the area through which emission of radiation from the keyhole occurs, as indicated by the white areas in Fig. 1, resulting in a significant drop of the overall absorptance [1, 8, 9]

$$\eta_A = \frac{P_A}{P_L} \tag{1}$$

✉ Jonas Wagner
jonas.wagner@ifsw.uni-stuttgart.de
http://www.ifsw.uni-stuttgart.de

[1] Institut für Strahlwerkzeuge (IFSW), University of Stuttgart, Pfaffenwaldring 43, 70569 Stuttgart, Germany

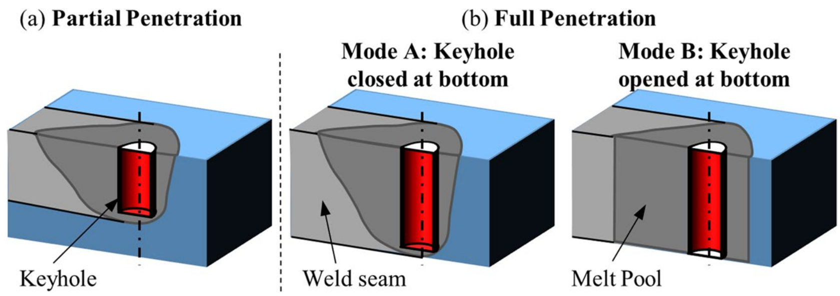

Fig. 1 Comparison of partial-penetration (**a**) and the two modes of full-penetration (**b**) laser welding

which is given by the ratio between the total power P_A that is absorbed in the processed material and the incident laser power P_L. The absorptance primarily depends on the absorptivity A of the processed material, the wavelength of the laser radiation, and the geometry of the interaction zone [10, 11]. Changes of the geometry of the keyhole therefore provoke changes of the absorptance and vice versa. It is known that the occurrence of these changes often results in instabilities of the welding process which can lead to the formation of pores [12–14], spatters [15, 16], and fluctuations of the depth of the weld seam [14]. It was shown by means of numerical simulations [17] that this may lead to an unstable process with alternating opening and closing of the keyhole at the bottom side of the sheet when the absorbed laser power is not sufficient for a reliable full-penetration process in *mode B*. This is also indicated by the results in [18] where a stochastic opening and closing of a *full-penetration hole*, i.e., a keyhole which is opened at the top and the bottom, was observed. Knowledge about the change of the absorptance at the transition from partial- and full-penetration *mode A* to full-penetration laser welding with a keyhole that is opened at its bottom is thus of great importance for the choice of appropriate process parameters to prevent defects in the beginning of the weld seam.

Only a few experimentally [1, 9] and numerically determined [8] values of the absorptance associated with a reliable full-penetration welding have been reported to date. The change of the absorptance during the transition from partial- to full-penetration welding, which each full-penetration process must necessarily undergo, was not yet quantified.

The instability of the process at the transition between partial- and full-penetration mode hampers an accurate measurement of the change of the absorptance at this threshold by means of calorimetric experiments. In order to determine the change of the absorptance by calculating the beam propagation and the Fresnel absorption inside the vapor capillary, the geometry of the keyhole needs to be known at any given state of the process. For the present study, we therefore have determined the geometries of the keyholes by means of high-speed X-ray imaging of the running welding process, from which the 3D geometry of the keyholes was reconstructed applying simple assumptions on their symmetry. This allows to calculate the absorptance and distinctly distinguish between partial-penetration and full-penetration welding also very close to the transition. To the best of our knowledge, this is the first attempt to quantitatively analyze the changes of the absorptance at and near the transition from partial- to full-penetration laser welding.

2 Experimental setup

The experimental setup used for the time-resolved determination of the shape of the vapor capillary is shown in Fig. 2. The welded sample (blue) which is held by the clamping device (light gray) is moved with a constant velocity of $v = 6$ m/min in negative x-direction below the stationary laser optics (dark gray). The X-ray beam (light green) is generated in an X-ray tube (green) and propagates through the sample in negative y-direction where it is locally attenuated depending on the thickness of the transirradiated material. The X-ray radiation emerging from the rear side of the sample is converted into visible light by a scintillator and

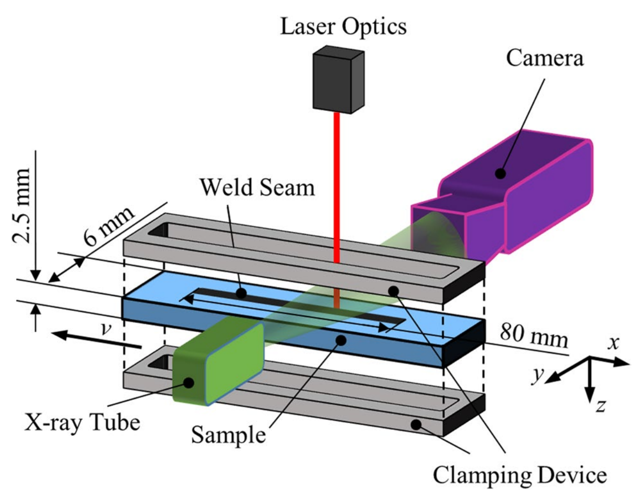

Fig. 2 Setup for the X-ray imaging of the keyholes during partial- and full-penetration laser welding. The parts of the clamping device are shown in a position separated from the welded sample to better illustrate the complete arrangement

subsequently amplified by an image intensifier. The thus created image is recorded by a high-speed camera (purple) with 1000 frames per second and a spatial resolution of 64 pixels/mm. The acceleration voltage of the X-ray tube was set to 60 kV and the power was 90 W. The X-ray facility is described in detail in [19].

In order to focus on the investigation of the change of the absorptance at the transition from partial- to full-penetration welding and to exclude a potential influence of a gap, all welds were conducted on single sheets. The aluminum alloy AA6014 was used with a thickness of $s_0 = 2.5$ mm. As sketched in Fig. 2, the samples had a length of 100 mm and a width of 6 mm. The length of the weld seams was 80 mm. The X-ray tube and the imaging system were positioned such that the capillary was horizontally (x-axis) centered in the recorded images and that the bottom edge of the samples can be clearly identified. The upper 0.5 mm of the sample and the observed capillaries could not be seen on the X-ray images due to an aperture in the imaging system. The laser optics had a magnification of 1:1 and a focal length of 200 mm. Different beam delivery fibers with core diameters of 100 µm, 400 µm, and 600 µm were applied in order to obtain different beam diameters on the workpiece. A TruDisk 8001 laser from TRUMPF was used in combination with the fiber with a core diameter of 100 µm and a TruDisk 16002 laser was used in the case of the application of the fibers with the core diameters of 400 µm and 600 µm. Both disk lasers operate at a wavelength of 1.03 µm. The setup resulted in diameters of the beam waist of $d_f = 100$ µm, $d_f = 400$ µm, and $d_f = 600$ µm with associated beam propagation factors of $M^2 = 15.25$, $M^2 = 61.00$, and $M^2 = 91.50$, respectively. The laser beam was always focused with its waist on the upper surface of the sample.

In order to enhance the image contrast and to reduce the noise, the obtained X-ray videos were post-processed with a flat field correction and Kalman filtering [20, 21].

3 Analysis of the transition between partial- and full-penetration welding

The changes of the capillary's geometry and especially of its length near the transition from partial-penetration to full-penetration welding were investigated by linearly ramping up the laser power P_L along the weld seam as shown in Fig. 3 for the three different beam diameters. The power was adjusted so that a keyhole which is closed at its bottom was observed in the X-ray images at the beginning of the process and a keyhole which is opened at its bottom was present at the end of the process. Apart from the beginning of the process, this resulted in a continuously visible weld seam at the bottom side of the sheet, which indicates a transition between the two different full-penetration modes (*mode A* and *mode B*) shown in Fig. 1b. The insets depict single frames from the X-ray videos at the corresponding time and laser power. The white dashed lines in the images were manually added to encircle the light areas and correspond to the estimated outline of the keyholes. The white dash-dotted line represents the beam axis assuming a distance of $d_f/2$ from the average position of the keyhole front.

The direction of the movement of the samples below the stationary laser optics is indicated by the white arrow v in the leftmost inset. All the three shown processes start with a keyhole which is closed at its bottom (1), either in full-penetration *mode A*, as sketched in Fig. 1b, in the case of welding with $d_f = 100$ µm or with partial-penetration, as sketched in Fig. 1a, in the case of welding with $d_f = 400$ µm and $d_f = 600$ µm. At slightly increased laser power, the process first only temporally changes to full-penetration *mode B* with a keyhole which is opened at its bottom, see (3) for $d_f = 600$ µm and (2) for both $d_f = 400$ µm and $d_f = 100$ µm. Despite the further increase of the laser power during the process, the keyhole temporarily closes again at its bottom in all cases, as shown with (4) for $d_f = 600$ µm; with (3), (4), and (5) for $d_f = 400$ µm; and with (3) and (5) for $d_f = 100$ µm. This can be explained by the fact that less power is absorbed when the capillary is open on the lower end and the welding process may fall back into partial-penetration mode when the deficiency of the absorbed power is too large. Reliable full-penetration welding in *mode B* is only achieved once the incident laser power is high enough (6) so that after a change of the absorptance evaporation temperature and a sufficiently high evaporation pressure are maintained and the absorbed power is not reduced to below the one that is needed to pierce through the workpiece.

The image sequences shown in Fig. 3 indicate that the majority of the keyhole fluctuations are characterized by the alternating opening and closing of the bottom of the keyhole during the transition from partial- to full-penetration welding. The initial transient formation of the keyhole occurs during the first 0.1 s of the process. The laser power at which full-penetration *mode B* is reached for the first time after this initial phase is referred to as full-penetration threshold P_{thr} for the remainder of the present report.

In order to determine the specific value of P_{thr}, the depth of the keyhole was analyzed during the linear increase of laser power by means of streak images. These images were generated by extracting only the pixel column at the position of the axis of the laser beam assuming a distance of $d_f/2$ from the average position of the keyhole front, indicated by the white dash-dotted lines in Fig. 3, from each frame of the video and lining them up chronologically from left to right in one picture, as shown in Fig. 4 using an example with $d_f = 600$ µm. The temporal evolution of the penetration depth was visually determined from the streak images by evaluating the contrast of the grayscale values as indicated

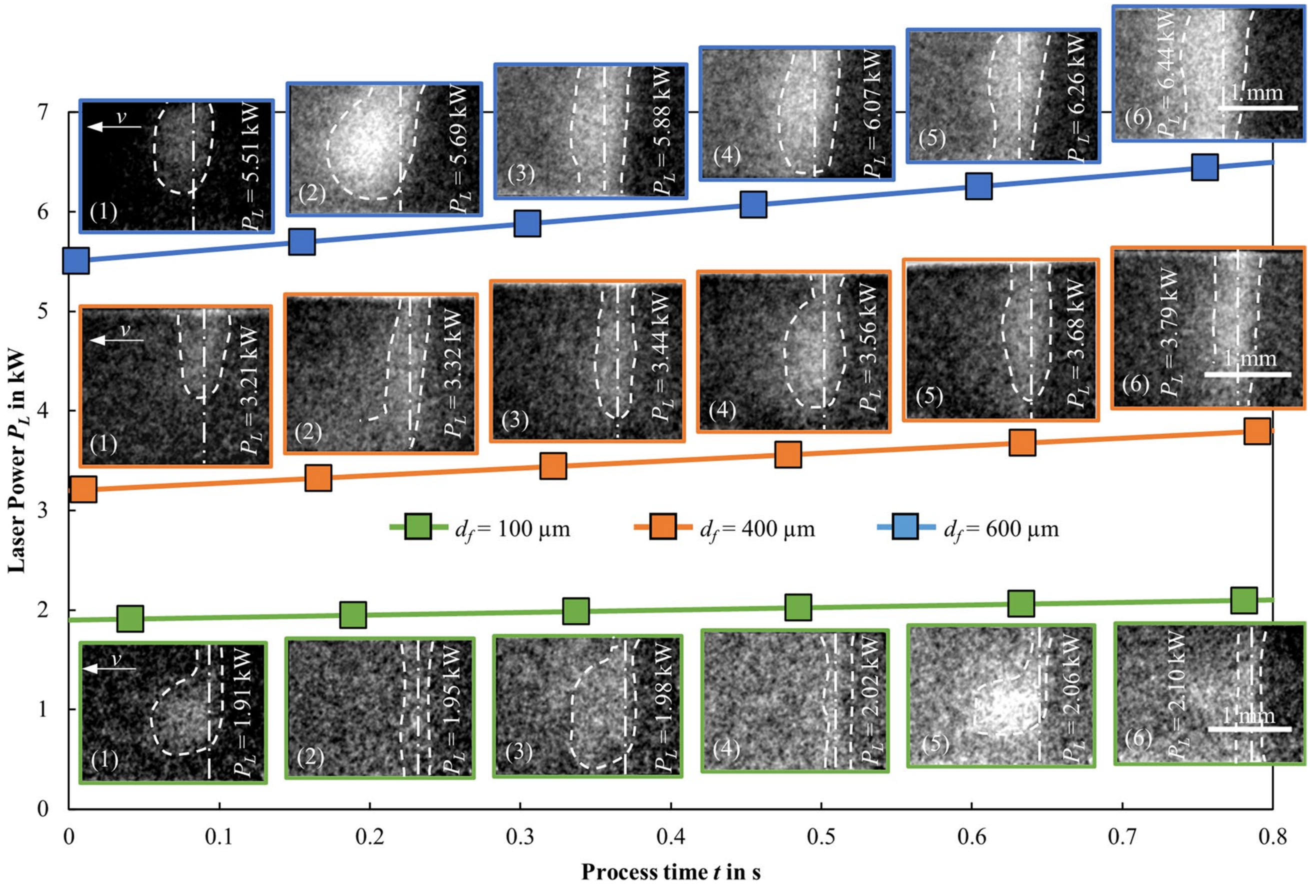

Fig. 3 Applied linearly increased laser power with corresponding X-ray images of the keyholes for three different focal beam diameters d_f on the surface of the workpiece; AA6014, $v = 6$ m/min, $s_0 = 2.5$ mm

by the dashed blue line and the left ordinate. The red line and the right vertical axis represent the corresponding laser power. The semi-transparent blue area in Fig. 4 marks the duration of the initial transient and often spiking formation of the keyhole which was excluded for this analysis to obtain reproducible results. The horizontal red dashed line indicates the threshold power of $P_{thr} = 5.9$ kW which was determined in this example, as indicated by the vertical dotted line.

The data points (round circles) in Fig. 5 represent the average values of P_{thr}, as determined from three experiments with each of the different beam diameters. The range between the minimum and maximum determined values is smaller than the extent of the circles. As the exact value may be influenced by the slope of the power ramp, i.e., the selection of P_{min} and P_{max} and the detection of the fluctuating opening of the keyhole is subject to some uncertainty, the maximum laser power which ensures persistent welding with a keyhole which is closed at its bottom (partial-penetration or welding in full-penetration *mode A*) is defined as $0.9 \cdot P_{thr}$ and the minimum laser power which ensures continuous full-penetration as $1.1 \cdot P_{thr}$. Consecutive trials with constant laser power,

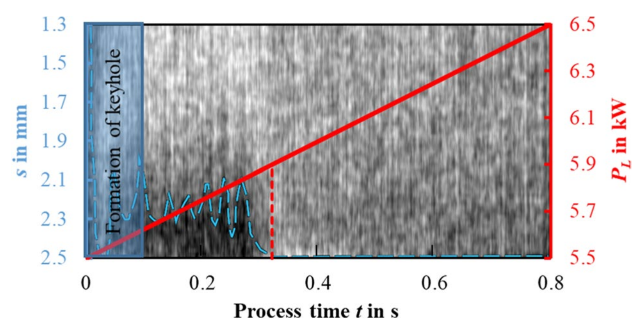

Fig. 4 Streak image showing the depth of the capillary at the position of the axis of the laser beam during welding of AA6014 with a linear increase of the incident laser power from $P_{min} = 5.5$ kW to $P_{max} = 6.5$ kW, $v = 6$ m/min, $d_f = 600$ µm, $s_0 = 2.5$ mm. In this example, the threshold to full-penetration welding in *mode B* was found to be $P_{thr} = 5.9$ kW

which are described in the following section, confirmed that the determined powers result in the corresponding keyhole behavior.

The segments in Fig. 5 represent the different regimes during laser beam welding. The lowest segment in Fig. 5

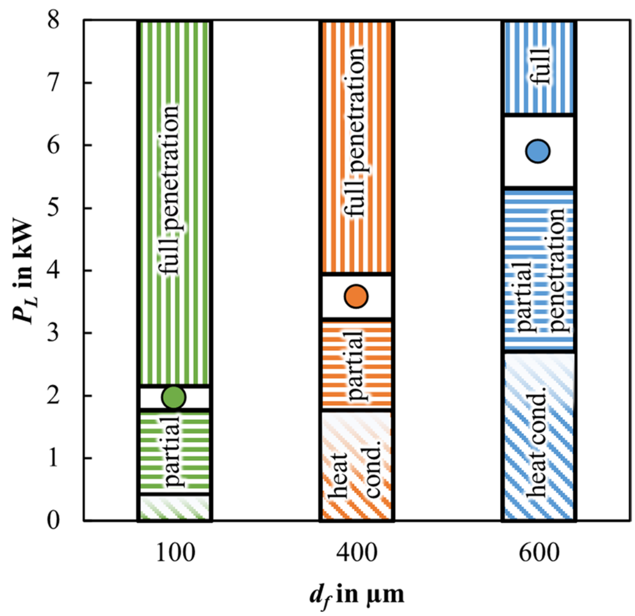

Fig. 5 Power-dependent welding regimes when welding 2.5-mm-thick AA6014 sheets with different beam diameters d_f. The circles correspond to the threshold power P_{thr} as averaged from three experiments

(diagonal hatching) represents heat-conduction welding without a keyhole. The faded upper range of this segment represents the range within which the deep-penetration threshold is estimated. Its upper limit is described by the power (of the top-hat shaped beam) at the deep-penetration threshold for welding of a semi-infinite body without heat accumulation [22]

$$P_{dp} = d_f \cdot \frac{\lambda_{th} \cdot (T_v - T_0)}{A} \cdot \frac{\pi^{\frac{3}{2}}}{4} \cdot \sqrt{\frac{Pe}{4} + 1.275}, \tag{2}$$

which was calculated for the given process parameters, where $Pe = \frac{d_f \cdot v \cdot \rho \cdot c_p}{\lambda_{th}}$ is the Peclet number, $\lambda_{\mathrm{th}} = 200\ \mathrm{W/(m \cdot K)}$ the heat conductivity of the welded material [23], $\rho = 2700\ \mathrm{kg/m^3}$ its density [23], $c_p = 896\ \mathrm{J/(kg \cdot K)}$ its heat capacity [23], $T_v = 2586$ K its evaporation temperature [24], $A = 0.12$ [25] its absorptivity, and $T_0 = 293$ K is the ambient temperature. The adjacent segment (horizontal hatching) ranges from P_{dp} to $0.9 \cdot P_{\mathrm{thr}}$ and represents the regime of persistent welding with a keyhole which is closed at its bottom, including partial-penetration and full-penetration *mode A*. The upper segment (vertical hatching) represents the regime of continuous full-penetration welding in *mode B* with $P_L \geq = 1.1 \cdot P_{\mathrm{thr}}$.

4 Change of absorptance

In order to analyze the change of the absorptance that occurs at the transition from partial to full penetration, the transient behavior of the keyhole was captured during welding with $P_L = 0.9 \cdot P_{\mathrm{thr}}$, $P_L = P_{\mathrm{thr}}$, and $P_L = 1.1 \cdot P_{\mathrm{thr}}$. The trials with $P_L = 0.9 \cdot P_{\mathrm{thr}}$ and $P_L = 1.1 \cdot P_{\mathrm{thr}}$ confirmed that reliable welding with a keyhole which is closed or opened at its bottom was achieved with the corresponding laser power. Figure 6 shows X-ray images of the keyhole at different moments in time during welding with a constant power of $P_L = P_{\mathrm{thr}}$ and $d_f = 600$ µm.

The direction of the movement of the sample below the stationary laser optics is indicated by the white arrow v. The welding process is seen to alternate between full-penetration *mode A* ($t = 30$ ms, $t = 330$ ms, $t = 480$ ms) and full-penetration *mode B* ($t = 180$ ms, $t = 630$ ms, $t = 780$ ms). This unstable process is common in the transitional power range near P_{thr} and evidences that a surplus of laser power is required

Fig. 6 Single frames at different times t from an X-ray video of laser welding of AA6014 with $P_L = P_{\mathrm{thr}} = 5.9$ kW, $v = 6$ m/min, $d_f = 600$ µm, and $s_0 = 2.5$ mm

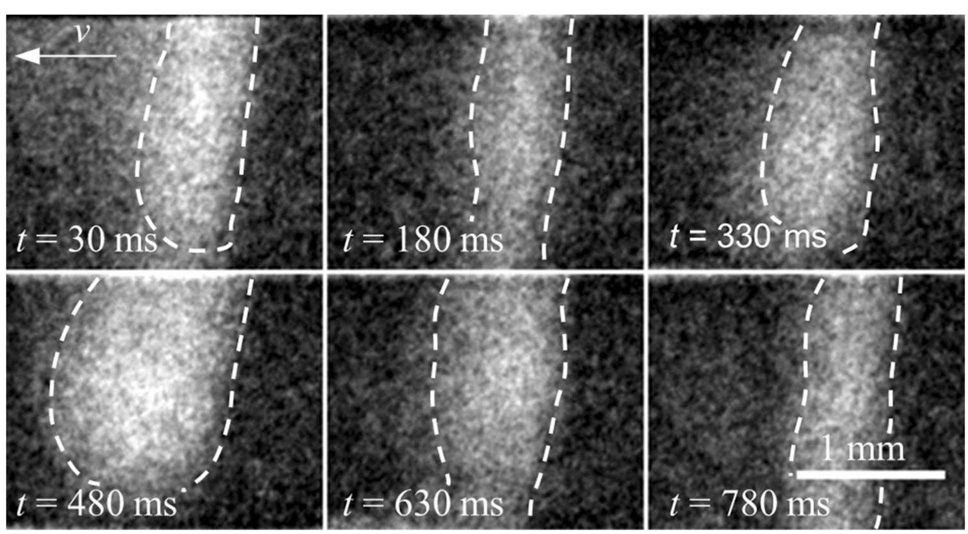

in order to achieve reliable full-penetration welding. The new findings from the X-ray videos agree well with previous results obtained by top-view records [18], which show that the full-penetration hole appears more frequently with increasing laser power, i.e., the fraction of time increases during which the keyhole is open at the bottom. The time between consecutive openings of the keyhole at the bottom of the welded sheet was observed to be in the order of several 10 ms.

For a quantitative evaluation, each experiment with the constant laser powers $P_L = 0.9 \bullet P_{thr}$, $P_L = P_{thr}$, and $P_L = 1.1 \bullet P_{thr}$ was repeated three times. In order to extract representative geometries of the keyholes, the frames of the corresponding high-speed X-ray videos for each trial were averaged over the time range starting at 100 ms after the beginning of the process and ending 100 ms before the end of the process, during which a constant temperature distribution can be assumed. As two states of the keyhole could be distinguished for $P_L = P_{thr}$, as shown in Fig. 6, two separate images were generated for the corresponding experiments: An average image considering only the frames where the keyhole was closed at the bottom and an average image considering only the frames in which the keyhole was opened at the bottom.

Figure 7 shows several examples of these averaged images to illustrate different regimes of the welding process with $d_f = 600$ µm.

The 3D geometry of the keyholes was reconstructed from the temporally averaged grayscale images for each trial as described in [1, 14, 26] using the attenuation coefficient $\mu = 0.125$ mm^{-1} for the X-ray probe beam as determined in [26]. In order to account for the upper 0.5 mm of the capillary which could not be observed in the recorded images, the upper 0.2 mm of the capillary reconstructed from its visible part was stretched by a factor of 3.5 in negative z-direction. This procedure is illustrated in the top row in Fig. 8, which compares the reconstructed geometry without correction (black outline) and the adapted capillary geometry (representation of the surface) to account for its real length. The black dashed horizontal line represents the lower boundary of the region which was elongated. The geometry below the black dashed line was kept unaltered and corresponds to the measured shape of the capillary. An overview of all reconstructed and adapted keyholes is given by Fig. 12 in the Appendix.

The distribution of the irradiance absorbed at the inner surface of these reconstructed keyholes was calculated by means of raytracing with the algorithm described in [27]. The bundle of the rays incident at the upper opening of the reconstructed keyhole was defined according to the specifications of the used laser beams, which always exhibited a top-hat shaped intensity distribution in the focal plane. It was assumed that the distance between the front of the keyhole and the beam axis equals $d_f/2$. The propagation of 500,000 randomly polarized rays was calculated considering up to 25 specular reflections of each ray on the surface of the reconstructed keyholes. The complex refractive index $n_c = 4.5 - i \cdot 9.0$ of liquid aluminum at $T = 2500$ °C [28] was used to calculate the Fresnel absorption at each reflection of the rays on the walls of the keyhole.

The total power P_A that is absorbed within the keyholes was calculated as the sum of the powers absorbed at each reflection of a ray. From this, the total absorptance η_A was calculated according to Eq. (1) for each reconstructed keyhole. Subsequently, the absorptance for each set of parameters was calculated as the arithmetic mean of the absorptance in the three corresponding keyholes.

In order to derive the absorptance during welding at the threshold with $P_L = P_{thr}$, the absorptances for both observed states of the keyhole were calculated separately. With these values, a weighted arithmetic mean of the absorptance was calculated according to the duration that each mode was present during welding the complete seam.

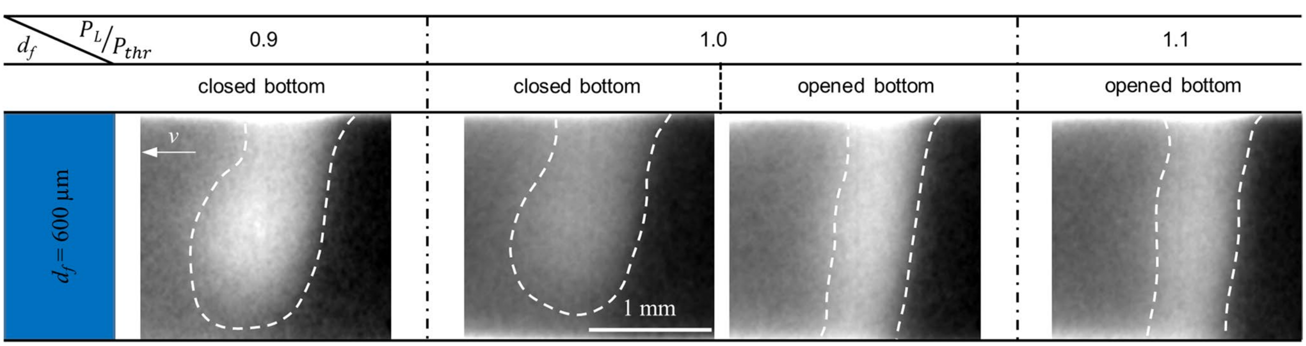

Fig. 7 Averaged X-ray images of the vapor capillary during laser welding of AA6014 in the different process regimes. Persistent partial-penetration/full-penetration *mode A* (left), transitional regime (two pictures in the center), continuous full-penetration *mode B* (right). With $P_{thr} = 5.9$ kW, $v = 6$ m/min, $d_f = 600$ µm, and $s_0 = 2.5$ mm

4.1 Determination of the change of the absorptance

The table in the top of Fig. 8 shows representative examples of reconstructed keyholes for each welding mode for $d_f = 600$ µm. The distribution of the absorbed irradiance is shown by the color-coded surface as given by the logarithmic scale shown on the right of Fig. 8 and the total absorptance η_A of the corresponding keyhole is denoted below each of the depicted geometries. The heights of the bars in the chart in the lower part of Fig. 8 represent the total absorptances which were each averaged over the three trials, corresponding to each set of parameters. The diagonally hatched bars represent the absorptance of the keyholes which are closed at their bottom and the fully colored bars represent the absorptance of keyholes that are opened at the bottom. For welding at the threshold with $P_L = P_{thr}$, the two bars representing the corresponding average absorptance during each mode are superimposed and the squared data points denote the weighted mean of the absorptance according to

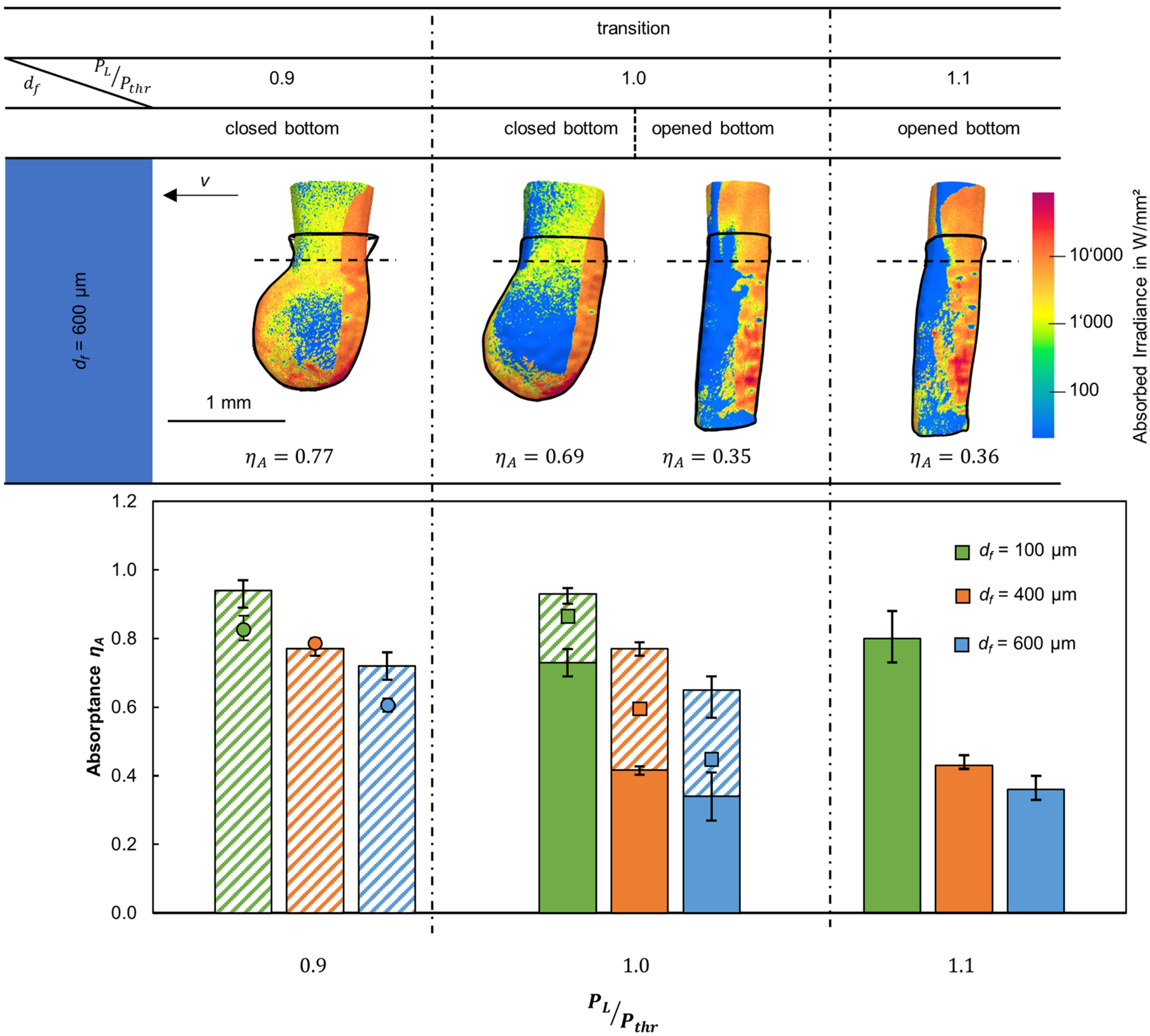

Fig. 8 Geometries of the keyholes and calculated absorptances for three different laser powers P_L and three different beam diameters d_f. Top: reconstructed keyholes for welding with $d_f = 600$ µm, as observed in the recorded images (black outline) and with adapted length (colored surface), with calculated distribution of the absorbed irradiance (color coded) and total absorptances η_A. Bottom: total absorptances as determined by raytracing; diagonally hatched bars for keyholes which are closed at the bottom and fully colored bars for keyholes which are opened at the bottom, squared data points for weighted mean at $P_L = P_{thr}$, and circular data points as determined with Gouffé's analytical model [10, 11]. $P_{thr} = 5.9$ kW for $d_f = 600$ µm, $P_{thr} = 3.6$ kW for $d_f = 400$ µm, and $P_{thr} = 2.0$ kW for $d_f = 100$ µm, AA6014, $s_0 = 2.5$ mm

the duration that each mode was present. The length of the error bars represents the range between the minimum and maximum determined absorptance for each set of parameters. The corresponding data and images of the reconstructed keyholes are given by Fig. 12 in the Appendix. The circular data points represent analytically calculated absorptances for $P_L = 0.9 \cdot P_{\mathrm{thr}}$, which are described in detail further below.

The data shows that the absorptance is highest for the small beam diameter $d_f = 100$ µm (on the sample's surface) for all welding modes and that the absorptance decreases with increasing beam diameter. A significant decrease of absorptance during the transition from partial to full penetration (from $P_L = 0.9 \cdot P_{\mathrm{thr}}$ to $P_L = 1.1 \cdot P_{\mathrm{thr}}$) and high fluctuations at the threshold, as shown by the large difference between the diagonally hatched and the fully colored bars at $P_L = 1.0 \cdot P_{\mathrm{thr}}$, are observed for all three values of d_f.

For comparison with the raytracing results, the absorptance during full-penetration *mode A* was additionally calculated by means of the slightly corrected analytical model [10] that was originally introduced by Gouffé [11]. This model is limited to the calculation of the absorptance of keyholes which are closed at the bottom. The analytical model calculates the absorptance

$$\eta_A = A \frac{1 + (1 - A)\left(\frac{o_{\mathrm{top}}}{O_{\mathrm{total}}} - \frac{\Omega}{2\pi}\right)}{A\left(1 - \frac{o_{\mathrm{top}}}{O_{\mathrm{total}}}\right) + \frac{o_{\mathrm{top}}}{O_{\mathrm{total}}}} \tag{3}$$

based on the material's absorptivity A and the geometric features of the keyhole, where o_{top} is the area of the keyhole's opening, O_{total} is the complete surface area of the keyhole consisting of the opening o_{top}, and the keyhole walls at the side and bottom, and Ω is the solid angle corresponding to the field of view of the keyhole's opening as seen from the center of the irradiated surface at the bottom of the keyhole. In most applications of the model, the keyhole is assumed to have the shape of a cylinder, due to usually missing information on the actual geometry. For the comparison presented here, the analytical model is applied to experimentally determined geometries and o_{top} and O_{total} were determined directly from the reconstructed 3D geometries of the keyholes. The solid angle Ω was approximated by

$$\Omega \approx o_{\mathrm{top}} / s^2, \tag{4}$$

where s is the depth of the keyhole. Assuming an absorptivity of $A = 0.12$ [25], this yields the values represented by the circular data points in the bottom left of Fig. 8. For $d_f = 600$ µm and $d_f = 100$ µm, the analytical model yields an absorptance which is approximately 0.1 lower than the one obtained by raytracing. For $d_f = 400$ µm, only a minor deviation between both methods is observed. Possible reasons for the deviations between the results of the two approaches are an uncertainty regarding the absorptivity and the complex refractive index for liquid aluminum at evaporation temperature and the different assumptions made in the model and the raytracing algorithm. One major difference is that diffuse reflection is assumed after the initial reflection in Gouffé's model, whereas the raytracing algorithm considers specular reflection. The second difference is that in Gouffé's model it is assumed that the incident laser radiation initially irradiates a part of the capillary which is far away from the opening, whereas in the raytracing algorithm it irradiates the wall of the capillary to a significant extent already in the upper part near the opening.

With the values of the absorptance determined from the raytracing calculations, the relative drop in absorptance that occurs during the transition from partial- to full-penetration welding was calculated by

$$\delta\eta_A = 1 - \frac{\eta_A\left(1.1 \cdot P_{\mathrm{thr}}\right)}{\eta_A\left(0.9 \cdot P_{\mathrm{thr}}\right)}. \tag{5}$$

The results are shown in Fig. 9, where the height of the bars represents the relative decrease $\delta\eta_A$ for each of the three considered diameters d_f of the beam waist. The error bars indicate the minimum and maximum values resulting from the minimum and maximum values of $\eta_A\left(1.1 \cdot P_{\mathrm{thr}}\right)$ and $\eta_A\left(0.9 \cdot P_{\mathrm{thr}}\right)$ as given by the error bars in Fig. 8.

The results show a significant decrease of absorptance for all the three considered values d_f. This decrease is less pronounced for the small beam diameter $d_f = 100$ µm and increases with increasing beam diameter. It is assumed that the extent of the relative decrease is associated with the aspect ratio s_0 / d_f. At low aspect ratios, the share of the bottom area in the total irradiated area is high, resulting in a large drop in the absorptance after piercing through

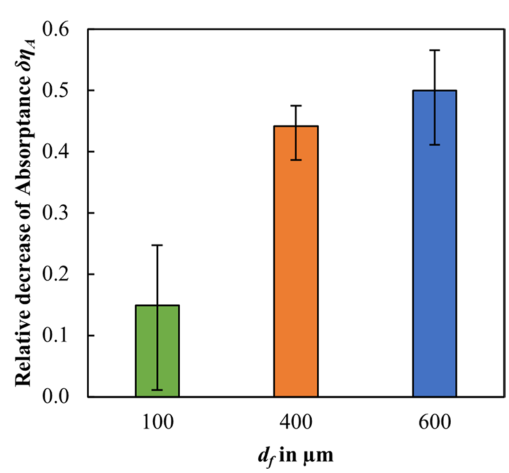

Fig. 9 Relative decrease $\delta\eta_A$ of the absorptance during the transition from partial- to full-penetration welding with $s_0 = 2.5$ mm, AA6014, $v = 6$ m/min

the bottom of the sheet. At high aspect ratios, the share of the bottom area in the total area and therefore the relative decrease of absorptance during the transition is reduced.

4.2 Discussion of the absorptance at powers exceeding the full-penetration threshold

A surplus of laser power is commonly applied to ensure reliable laser welding in the full-penetration mode by avoiding the instabilities that otherwise occur at powers close to the threshold value. In an industrial context, it is often not practical to determine the minimal laser power which ensures reliable full-penetration welding. Additionally, a high tolerance to variations of the process environment and the material properties is particularly important, which is why laser powers are commonly applied that significantly exceed the value of $1.1 \cdot P_{\mathrm{thr}}$ that was considered above. In order to describe the absorptance during industrial full-penetration laser welding applications, it is therefore expedient to also consider the influence of an increasing laser power well beyond $1.1 \cdot P_{\mathrm{thr}}$. In order to determine the dependence of the absorptance for full-penetration welding with increased power, the keyholes during welding with $P_L = 1.2 \cdot P_{\mathrm{thr}}$ and $P_L = 1.3 \cdot P_{\mathrm{thr}}$ were also reconstructed and the absorptance was determined by means of raytracing as described above. Figure 10 shows all reconstructed keyholes which are opened at its top and its bottom for welding with $d_f = 600\ \mu\mathrm{m}$. The distribution of the absorbed irradiance is shown by the color-coded surface as given by the logarithmic scale shown on the right of Fig. 10.

The comparison of the reconstructed geometries in Fig. 10 shows that no significant change of the keyhole geometry occurs for $P_L \geq P_{\mathrm{thr}}$ within the investigated range of laser powers. Consequently, as indicated by the comparison of the color-coded areas in Fig. 10, no significant changes of the distribution of the absorbed irradiance occur with increasing laser power for $P_L \geq P_{\mathrm{thr}}$. This was also observed for welding with the other focal beam diameters of $d_f = 100\ \mu\mathrm{m}$ and $d_f = 400\ \mu\mathrm{m}$. The corresponding data and images of the reconstructed keyholes are given in Fig. 12 in the Appendix.

The absorptances during welding with a keyhole which is opened at its top and bottom for the different laser powers (average over three trials) are represented by the diamond-shaped data points in Fig. 11. The corresponding error bars represent the minimum and maximum values determined in three trials. Each of the dashed-dotted lines in Fig. 11 represents the mean absorptance of all experimentally determined keyholes which are opened at the bottom for the corresponding d_f. The variation as indicated by the scatter band was derived by averaging only the minimum and maximum values of the respective determined absorptances as represented by the error bars of the data

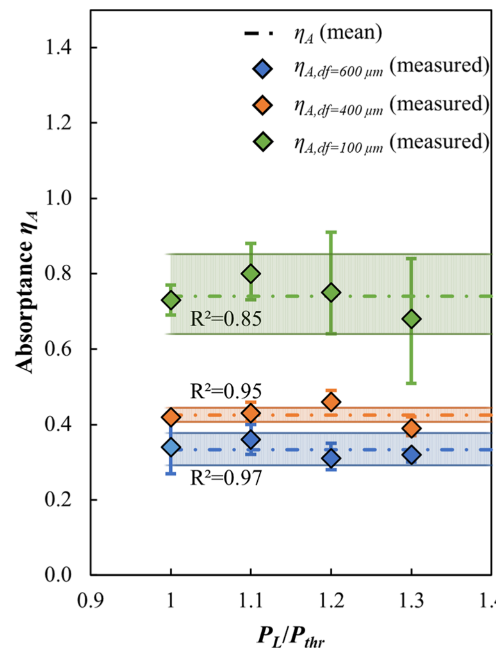

Fig. 11 Absorptance in keyholes which are opened at its top and bottom during welding of AA6014 with $P_L \geq P_{\mathrm{thr}}$. Experimental results (data points) and corresponding mean values (dashed-dotted lines)

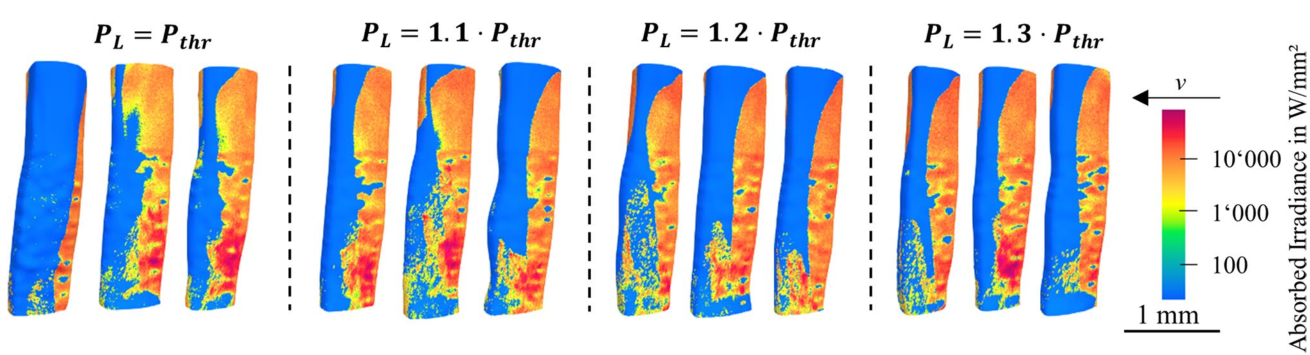

Fig. 10 Reconstructed geometries of the keyholes with calculated distribution of the absorbed irradiance (color coded) for different laser powers $P_L \geq P_{\mathrm{thr}}$ with $d_f = 600\ \mu\mathrm{m}$, $P_{\mathrm{thr}} = 5.9$ kW, AA6014, and $s_0 = 2.5$ mm

points in Fig. 11. Additionally, the coefficients of determination R^2 are given to indicate the variation of the measured absorptances (data points) from the corresponding constant course of the absorptance (dashed-dotted line).

The values of R^2 close to 1 indicate that the absorptance is constant and independent of the irradiated laser power for $P_L \geq P_{\mathrm{thr}}$ within the investigated range of incident laser powers.

5 Implications on process stability

5.1 Beginning of the process

As shown in Fig. 6, the spontaneous drop of the absorptance impedes a stable welding process at the threshold. A reliable application of the full-penetration welding process therefore requires either a sophisticated closed-loop control as demonstrated in [18] or a surplus of laser power. At the beginning of the process, however, passing through this regime is unavoidable. X-ray records of the full-penetration welding show that the fluctuations of the capillary's geometry during the beginning of the process result in an excessive formation of pores [1, 29–31]. During the further progress of the process, a reliable full-penetration process is achieved with an increased stability of the geometry of the keyhole.

During partial-penetration welding, it was shown that keyholes, in which fluctuations in geometry result in strong variations in the locally absorbed irradiance and in strong variations in the absorptance, are associated with an unstable process and the formation of pores. Keyholes in which fluctuations in the geometry have only minor effects on the absorbed irradiance and the absorptance are associated with a stable process [14, 32]. With regard to the transition from partial to full penetration, it can be concluded that a larger drop of absorptance leads to higher fluctuations in the process. As shown with Fig. 9, the drop of the absorptance is more pronounced in the case of large beam diameters $d_f \geq 400$ µm. Unfortunately, remote laser welding in car body manufacturing requires optical components with long focal distances which result in comparably large diameters of the beam waist in the order of typically 600 µm. Hence, lasers with higher beam quality are required to reduce the beam diameter on the sample's surface to potentially reduce fluctuations of the geometry of the keyhole during the initial state of full-penetration welding processes. In the case of butt welds, the application of small focal diameters may cause conflicts, as often large keyhole diameters are used in order to achieve a wide melt pool to ensure a sufficient connection between the sheets and to enable a tolerance to misalignments. In this case, based on the new findings presented here, the application of beam oscillation is recommended, to maintain a small keyhole diameter while archiving a wide melt pool through transversal movement of the keyhole [12, 33, 34].

5.2 During the process

A surplus of laser power exceeding the power at the threshold P_{thr} is required after the initial phase for a reliable application of the full-penetration welding process. If reliable full-penetration welding is ensured, the independence of the absorptance from the incident laser power above the full-penetration threshold results in differences of the characteristics of the process compared to partial-penetration welding.

During stable partial-penetration welding, the laser power, the keyhole geometry, and the absorbed laser power are directly related to each other. Consequently, changes in of these values also lead to changes in the other values and may result in a self-reinforcing, non-linear effect. E.g., a reduced incident laser power may lead to a reduced keyhole length and therefore a reduced aspect ratio which results in a decrease of the absorptance. Consequently, the absorbed laser power decreases to a greater extent than the reduction of the incident laser power. In the case of full-penetration welding, however, the new findings presented here show that the same change in laser power has only a linear effect on the absorbed laser power due to the constant absorptance as long as it is ensured that the laser power exceeds the value of the full-penetration threshold. This implies that full-penetration welding is more robust to fluctuations of the laser power and the keyhole geometry than partial-penetration welding.

The effect that a variation of the incident laser power at $P_L \geq P_{\mathrm{thr}}$ and therefore of the absorbed laser power has on the process result was not part of the presented investigations and requires further studies. Possible effects might be variations in the width of the melt pool and in the overheating of the melt or in the process efficiency due to different losses by spatter and vapor ejection.

6 Conclusion

The transition of the welding mode from partial to full penetration results in a significant decrease of the absorptance due to the formation of the second opening of the keyhole at its bottom. This drop of absorptance is more pronounced for larger focal diameters and is reflected by an unstable behavior of the keyhole, which was identified at the threshold between the two welding modes. Therefore, for a reliable application of the full-penetration welding process, a surplus of laser power is required. During the initial state of the formation of the keyhole in full-penetration laser welding with the inherent occurrence of instabilities, one can recommend the application of laser beams with small focal diameters. The influence of the transition on the formation of spatters and on the surface quality will be subject to future research.

Appendix

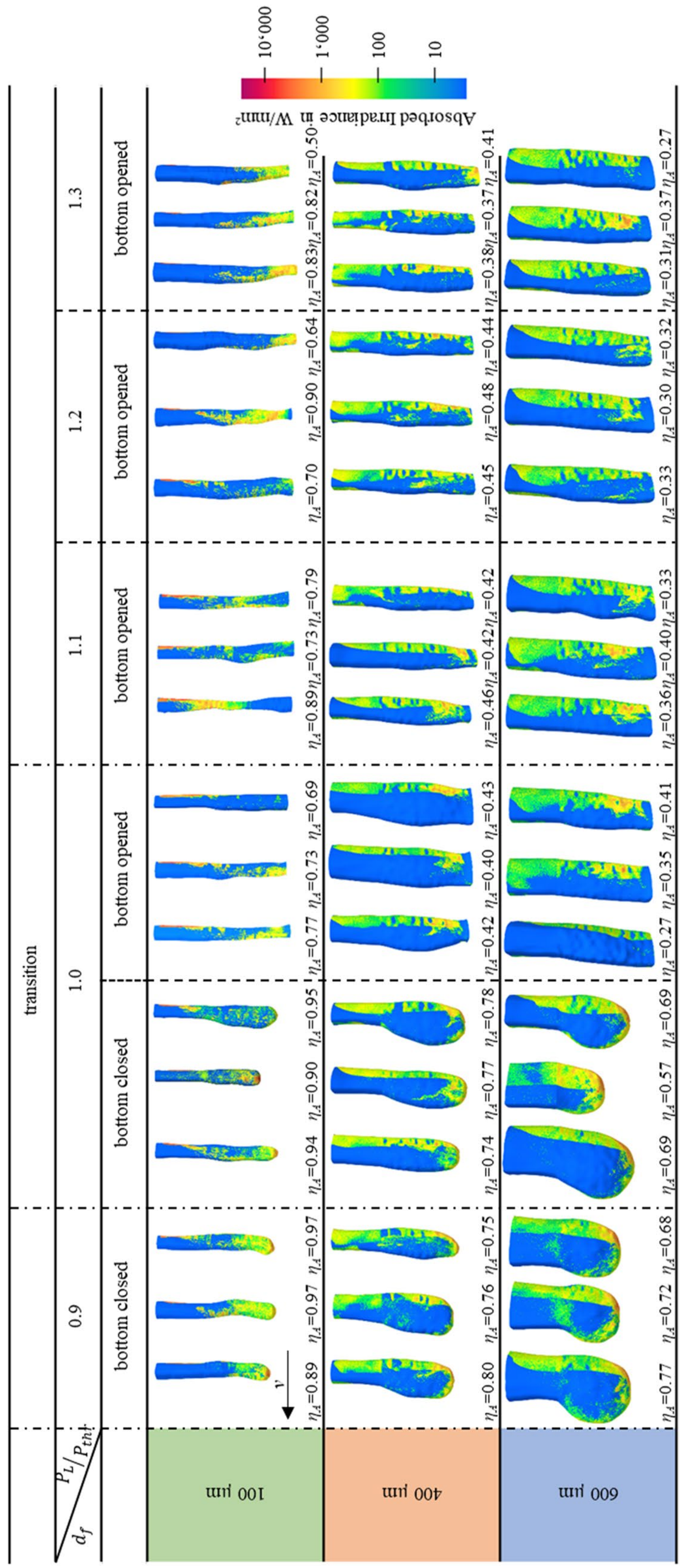

Fig. 12 Reconstructed keyhole geometries with calculated distribution of the absorbed irradiance (color coded) and calculated absorptances (below). $P_{thr} = 5.9$ kW for $d_f = 600$ µm, $P_{thr} = 3.6$ kW for $d_f = 400$ µm, and $P_{thr} = 2.0$ kW for $d_f = 100$ µm, AA6014, $s_0 = 2.5$ mm, $v = 6$ m/min

Author contribution All authors contributed to the study conception. Methodology, data curation, conceptualization, and writing—original draft preparation were performed by Jonas Wagner. Supervision and writing—reviewing were performed by Christian Hagenlocher, Rudolf Weber, and Thomas Graf. All authors read and approved the final manuscript.

Funding Open Access funding enabled and organized by Projekt DEAL. This work was funded in parts by the Deutsche Forschungsgemeinschaft (DFG, German Research Foundation)—389369540 and was funded in parts by the Deutsche Forschungsgemeinschaft (DFG, German Research Foundation)—398552773. The Laser beam source TruDisk8001 (DFG object number, 625617) was funded by the Deutsche Forschungsgemeinschaft (DFG, German Research Foundation)—INST 41/990–1 FUGG.

Declarations

Competing interests The authors declare no competing interests.

References

1. Wagner J, Hagenlocher C, Hummel M et al (2021) Synchrotron X-ray analysis of the influence of the magnesium content on the absorptance during full-penetration laser welding of aluminum. Metals 11:797. https://doi.org/10.3390/met11050797
2. Stritt P (2016) Prozessstrategien zur Vermeidung von Heißrissen beim Remote-Laserstrahlschweißen von AlMgSi 6016. Herbert Utz Verlag, München
3. Hagenlocher C, Lind J, Weber R et al (2020) High-speed X-ray investigation of pore formation during full penetration laser beam welding of AA6016 aluminum sheets contaminated with lubricants. Appl Sci 10:2077. https://doi.org/10.3390/app10062077
4. Chang B, Allen C, Blackburn J et al (2015) Fluid flow characteristics and porosity behavior in full penetration laser welding of a titanium alloy. Metall Mater Trans B 46:906–918. https://doi.org/10.1007/s11663-014-0242-5
5. Fabbro R, Slimani S, Coste F et al (2005) Study of keyhole behaviour for full penetration Nd–Yag CW laser welding. J Phys D: Appl Phys 38:1881–1887. https://doi.org/10.1088/0022-3727/38/12/005
6. Fetzer F, Stritt P, Berger P et al (2017) Fast numerical method to predict the depth of laser welding. J Laser Appl 29:22012. https://doi.org/10.2351/1.4983152
7. Fabbro R (2010) Melt pool and keyhole behaviour analysis for deep penetration laser welding. J Phys D: Appl Phys 43:445501. https://doi.org/10.1088/0022-3727/43/44/445501
8. Vázquez RG, Koch HM, Otto A (2014) Multi-physical simulation of laser welding. Phys Procedia 56:1334–1342. https://doi.org/10.1016/j.phpro.2014.08.059
9. Wang H, Nakanishi M, Kawahito Y (2017) Effects of welding speed on absorption rate in partial and full penetration welding of stainless steel with high brightness and high power laser. J Mater Process Technol 249:193–201. https://doi.org/10.1016/j.jmatprotec.2017.06.014
10. Hügel H, Graf T (2023) Materialbearbeitung mit laser: grundlagen und verfahren, 5th edn. Springer Fachmedien Wiesbaden, Wiesbaden
11. Gouffé A (1945) Corrections d'ouverture des corps-noirs artificiels compte tenu des diffusions multiples internes. Rev Opt 24:1–7
12. Fetzer F, Sommer M, Weber R et al (2018) Reduction of pores by means of laser beam oscillation during remote welding of AlMgSi. Opt Lasers Eng 108:68–77. https://doi.org/10.1016/j.optlaseng.2018.04.012
13. Matsunawa A, Mizutani M, Katayama S et al (2003) Porosity formation mechanism and its prevention in laser welding. Weld Int 17:431–437. https://doi.org/10.1533/wint.2003.3138
14. Fetzer F, Hagenlocher C, Weber R et al (2021) Geometry and stability of the capillary during deep-penetration laser welding of AlMgSi at high feed rates. Opt Laser Technol 133:106562. https://doi.org/10.1016/j.optlastec.2020.106562
15. Heider A, Sollinger J, Abt F et al (2013) High-speed X-ray analysis of spatter formation in laser welding of copper. Phys Procedia 41:112–118. https://doi.org/10.1016/j.phpro.2013.03.058
16. Li S, Chen G, Zhang M et al (2014) Dynamic keyhole profile during high-power deep-penetration laser welding. J Mater Process Technol 214:565–570. https://doi.org/10.1016/j.jmatprotec.2013.10.019
17. Bailey NS, Tan W, Shin YC (2015) A parametric study on laser welding of magnesium alloy AZ31 by a fiber laser. J Manuf Sci Eng 137. https://doi.org/10.1115/1.4029052
18. Blug A, Abt F, Nicolosi L et al (2012) The full penetration hole as a stochastic process: controlling penetration depth in keyhole laser-welding processes. Appl Phys B 108:97–107. https://doi.org/10.1007/s00340-012-5104-8
19. Abt F, Boley M, Weber R et al (2011) Novel X-ray system for in-situ diagnostics of laser based processes – first experimental results. Phys Procedia 12:761–770. https://doi.org/10.1016/j.phpro.2011.03.095
20. Diebold FX (1992) Forecasting, structural time series models and the Kalman filter, Andrew C. Harvey Cambridge University Press, 1939 - Fore casting, structural time series models and the Kalman filterAdrew C. Harvey Cambridge University Press, 1989. Econ Theory 8:293–299. https://doi.org/10.1017/S0266466600012822
21. Kalman RE (1960) A new approach to linear filtering and prediction problems. J Basic Eng 82:35–45. https://doi.org/10.1115/1.3662552
22. Graf T, Berger P, Weber R et al (2015) Analytical expressions for the threshold of deep-penetration laser welding. Laser Phys Lett 12:56002. https://doi.org/10.1088/1612-2011/12/5/056002
23. Kammer C (1998) Aluminium-Taschenbuch, 15th edn. Aluminium-Verlag, Düsseldorf
24. Rapp H-J (1996) Laserschweißeignung Von Aluminiumwerkstoffen Für Anwendungen Im Leichtbau. Laser in der Materialbearbeitung. Vieweg+Teubner Verlag, Wiesbaden
25. Dausinger F (1995) Strahlwerkzeug Laser: Energiekopplung und Prozesseffektivität. Laser in der Materialbearbeitung. Teubner, Stuttgart
26. Lind J, Fetzer F, Hagenlocher C et al (2020) Transition from stable laser fusion cutting conditions to incomplete cutting analysed with high-speed X-ray imaging. J Manuf Process 60:470–480. https://doi.org/10.1016/j.jmapro.2020.10.068

27. Qin Y, Michalowski A, Weber R et al (2012) Comparison between ray-tracing and physical optics for the computation of light absorption in capillaries–the influence of diffraction and interference. Opt Express 20:26606–26617. https://doi.org/10.1364/OE.20.026606
28. Hügel H, Graf T (2014) Laser in der Fertigung: Grundlagen der Strahlquellen, Systeme, Fertigungsverfahren, 3rd edn. Lehrbuch. Springer Vieweg, Wiesbaden
29. Wagner J, Hagenlocher C, Weber R, Hummel M, Beckmann F, Moosmann J, Graf T (2024) Synchrotron x-ray video of full-penetration laser welding of aluminum AA1050A. https://doi.org/10.18419/darus-3860
30. Chung W-S, Häusler A, Hummel M et al (2022) In-situ x-ray phase contrast observation of the full penetration spot welding on limited aluminum material thickness. J Laser Appl 34:42019. https://doi.org/10.2351/7.0000772
31. Chung W-S, Hummel M, Spurk C et al (2024) In situ X-ray phase contrast imaging of the melt and vapor capillary behavior during the welding regime transition on aluminum with limited material thickness. Weld World 68:43–50. https://doi.org/10.1007/s40194-023-01616-1
32. Hummel M, Hagenlocher C, Haeusler A et al (2023) Analysis on the influence of vapor capillary aspect ratio on pore formation in laser beam welding of aluminum. J Mater Process Technol 312:117862. https://doi.org/10.1016/j.jmatprotec.2023.117862
33. Jarwitz M, Fetzer F, Weber R et al (2018) Weld seam geometry and electrical resistance of laser-welded, aluminum-copper dissimilar joints produced with spatial beam oscillation. Metals 8:510. https://doi.org/10.3390/met8070510
34. Horník P, Šebestová H, Novotný J et al (2022) Laser beam oscillation strategy for weld geometry variation. J Manuf Process 84:216–222. https://doi.org/10.1016/j.jmapro.2022.10.016

Publisher's Note Springer Nature remains neutral with regard to jurisdictional claims in published maps and institutional affiliations.